ELSEVIER

Contents lists available at ScienceDirect

Acta Materialia

journal homepage: www.elsevier.com/locate/actamat



Full length article

Mechanically induced ferroelectric switching in BaTiO₃ thin films



Bo Wang^{a,*}, Haidong Lu^b, Chung Wung Bark^c, Chang-Beom Eom^c, Alexei Gruverman^b, Long-Qing Chen^{a,*}

- ^a Materials Research Institute, The Pennsylvania State University, University Park, PA 16802, USA
- ^b Department of Physics and Astronomy, University of Nebraska, Lincoln, NE 68588, USA
- ^c Department of Materials Science and Engineering, University of Wisconsin-Madison, Wisconsin 53706, USA

ARTICLE INFO

Article History: Received 17 September 2019 Revised 18 March 2020 Accepted 15 April 2020 Available online 3 May 2020

Keywords: Domain switching Flexoelectric effect Ferroelectric thin film Phase-field simulation

ABSTRACT

The ability to reverse or switch the polarization of a ferroelectric thin film through a mechanical force under an atomic force microscopy (AFM) tip offers the exciting possibility of a voltage-free control of ferroelectricity. One of the important metrics for characterizing such a switching process is the critical force F_c required to reverse a polarization. However, the experimentally measured values of F_c display a large uncertainty and vary significantly even for the same ferroelectric film. Here, using BaTiO₃ thin films as a model system, we systematically evaluate F_c using a combination of AFM-based experiments and phase-field simulations. In particular, we study the influence of the AFM tip radius, misfit strain, and film thickness on F_c as well as the interplay between the flexoelectric and piezoelectric effects. This work provides a deeper understanding on the mechanism and control of mechanically induced ferroelectric switching and thus guidance for exploring potential ferroelectric-based nanodevices based on mechanical switching.

 $\hbox{@ 2020 Published}$ by Elsevier Ltd on behalf of Acta Materialia Inc.

1. Introduction

Ferroelectric materials are characterized by the presence of a spontaneous polarization that can be reversibly switched using an electric field. Their applications include non-volatile random-access memories [1], electromechanical transducers [2], and electro-optical devices [3]. In ferroelectric thin films, polarization can be locally probed or switched by applying a voltage bias through a probe tip, which has been utilized to image ferroelectric domain structures [4], characterize local electromechanical properties [5,6], probe domain switching kinetics [7,8], and engineer nanodomain structures [9].

Aside from electric fields, other external stimuli can also be utilized to manipulate the polarization direction in ferroelectrics. For example, magnetic fields have been employed to switch polarization in several multiferroic materials [10–12]. The chemical environment of a ferroelectric surface can be utilized to reorient polarization in ultrathin films [13–15]. Moreover, a nanoscale mechanical force under an atomic force microscopy (AFM) tip has been shown to write arrays of nanodomains in ultrathin BaTiO₃ films [16]. The mechanism of mechanical switching was primarily attributed to the flexoelectric effect [16,17], i.e., the electromechanical coupling between polarization and inhomogeneous mechanical strains [18,19], although other possible mechanisms were also proposed [20–22].

E-mail addresses: bzw133@psu.edu (B. Wang), lqc3@psu.edu (L.-Q. Chen).

Mechanical switching of ferroelectricity has stimulated extensive research interests, as it offers a possibility of voltage-free control of polarization and thus avoids undesired side-effects such as leakage, dielectric breakdown, and charge injection [16]. Many concepts of nanoelectromechanical devices mediated by mechanical approaches were proposed, including mechanically enhanced ferroelectric tunneling junctions [23], mechanically gated transistors [24,25], mechanical lithography of nanodomains in capacitors [26], mechanically control of ionic defects [27], mechanically selected multilevel data storage [28], and mechanically enabled bulk photovoltaic effects [29].

Mechanical switching of polarization by AFM tip pressing has been demonstrated in various ferroelectric systems including BaTiO₃ [16,30,31], PbTiO₃ and Pb(Zr,Ti)O₃ [32–34], BiFeO₃ [28,35,36], TbMnO₃ [37], Bi₅FeTi₃O₁₅ [38], SrBi₂Nb₂O₉ [39], and HfO₂ [40] thin films, ferroelectric-based capacitors [25,26], and free-standing ferroelectric polymers [41,42]. The minimal force required to induce 180degree ferroelectric switching, known as the critical force F_c (or the threshold loading force [16,30]), is frequently used to assess the barrier for a ferroelectric thin film to be mechanically switched [16,30,33], in analogy to the critical bias for electrically induced switching. In contrast to the critical bias, however, F_c is much less investigated and poorly understood. For instance, reported values of F_c vary significantly in different ferroelectrics, ranging from several tens of nN [41] to several μ N [26,30,33]. Even for the same system, e. g., a 5 nm-BaTiO₃ film grown on a SrTiO₃ substrate, the experimentally measured F_c values have a large variation [16,30]. On the other side, theoretical studies based on numerical simulations reveal that

^{*} Corresponding authors.

the film thickness [17,20,21,43], frictional shear strain [20,28,44,45], shape of the AFM tip [17], and epitaxial misfit strain [20,46] can drastically affect the mechanical switching process. However, there is a still a lack of systematic and quantitative analysis on how F_c is influenced by these factors.

Here, we performed AFM-based experiments and phase-field simulations to systematically investigate the effect of tip radius, film thickness, and epitaxial misfit strain on the F_c of mechanical switching of BaTiO₃ thin films with various thicknesses epitaxially grown on $SrTiO_3$ substrates. The experiments show that F_c is sensitive to the tip radius and varies with the film thickness in a nontrivial way. Phase-field simulations were performed to theoretically evaluate F_c . By evaluating the local polarization P as a function of the loading force F, we extracted the theoretical critical force and examined it as a function of the tip radius, misfit strain, and film thickness. The P-F curves obtained therein also reveal an interplay between flexoelectricity and piezoelectricity during a mechanical loading-unloading cycle, providing an additional understanding of the mechanism of mechanical switching. The simulation results compare reasonably well with present and previous experiments [30] while plausible explanations for some discrepancies are discussed.

The remnant part of the manuscript is structured as follows. In Section 2, we specify the details of experimental methods and the phase-field model of mechanical switching of ferroelectrics. In Section 3 we present the experimental results on F_c and their dependences on the tip radius and film thickness. In Section 4, we describe the computed values of F_c based on simulation results and their dependences on the tip radius, misfit strain, and film thickness. In Section 5, we discuss the discrepancies between the experimentally measured and theoretically calculated critical forces and elaborated on the nontrivial effect of the film thickness on F_c . Finally, we summarize our findings and remaining issues to be explored.

2. Methods

2.1. Experiments

Single-crystalline epitaxial ultrathin BaTiO₃ films were grown on atomically smooth TiO₂-terminated (001)-SrTiO₃ substrate with a 30-nm-thick La_{0.67}Sr_{0.33}MnO₃ layer acting as a bottom electrode. Both layers were grown by pulsed laser deposition with *in situ* monitoring using high-pressure reflection high energy electron diffraction for thickness control; details of sample preparation can be found elsewhere [16]. The switching experiments were performed on thin films of various thickness ranging from 4-unit-cell (u.c.) to 48-u.c. (1.6 \sim 20 nm). The compressively strained BaTiO₃ thin films were fully coherent with the substrate and possessed only out-of-plane polarization [47]. The mechanical switching utilizing the flexoelectric effect was studied using a commercial AFM system (MFP-3D, Asylum Research).

Polarization switching via mechanical means was performed in the conventional AFM contact mode by scanning a region with applied mechanical pressure induced by the AFM tip (PPP-EFM from Nanosensors), while both the tip and bottom electrode remained grounded [16,44]. Domain structures were visualized using conventional piezoresponse force microscopy (PFM) mode with ac modulation bias of 0.3 V in amplitude at 350 kHz with a low loading force of 25 nN, which has been shown not to affect the sample surface topography and the mechanically-written domains [16].

2.2. Phase-field method

Phase-field method has been extensively applied to predicting and understanding the formation and evolution of ferroelectric domains under external stimuli [48,49]. In a phase-field model, the spontaneous polarization P_i is used as the order parameter, the kinetics of which is usually assumed to be linear and relaxational although

dynamic phase-field models have recently been proposed [50], i.e.,

$$\frac{\partial P_i}{\partial t} = -L \frac{\delta \mathcal{F}}{\delta P_i},\tag{1}$$

where L is the kinetic coefficient related to the domain wall mobility. The total free energy $\mathcal F$ contains the contributions from the bulk, elastic, electric, gradient, flexoelectric, and surface energies, i.e.,

$$\mathcal{F} = \int_{V} (f_{bulk} + f_{elastic} + f_{electric} + f_{gradient} + f_{flexo}) dV + \int_{S} f_{surf} dS$$
 (2)

A detailed description of the first four terms on the right-hand side of Eq. (2) can be found in Ref. [48]. The flexoelectric energy density f_{flexo} is expressed as

$$f_{flexo} = \frac{1}{2} f_{ijkl} \left(\frac{\partial P_k}{\partial x_l} \varepsilon_{ij} - \frac{\partial \varepsilon_{ij}}{\partial x_l} P_k \right), \tag{3}$$

where ε_{ij} represents the strain tensor and f_{ijkl} the flexocoupling coefficient. By taking variational derivatives of Eq. (3) with respect to P_k , the flexoelectric energy density produces a driving force read as

$$\frac{\delta \int \int \int f_{\text{flexo}} dV}{\delta P_k} = -f_{ijkl} \varepsilon_{ij,l} = -E_k^{\text{flexo}} \tag{4}$$

where E_k^{flexo} stands for the flexoelectric field [19]. The fourth-rank flexocoupling tensor f_{ijkl} contains three independent components for the cubic symmetry and are usually denoted using the Voigt notation, i.e., $f_{11} = f_{1111}$, $f_{12} = f_{1122}$ and $f_{44} = 2f_{1221}$. Therefore, the out-of-plane flexoelectric field responsible for the 180-degree polarization reversal can be expressed as

$$E_{3}^{flexo} = f_{11} \frac{\partial \varepsilon_{33}}{\partial x_{3}} + f_{12} \left(\frac{\partial \varepsilon_{11}}{\partial x_{3}} + \frac{\partial \varepsilon_{22}}{\partial x_{3}} \right) + f_{44} \left(\frac{\partial \varepsilon_{23}}{\partial x_{2}} + \frac{\partial \varepsilon_{13}}{\partial x_{1}} \right). \tag{5}$$

On the other hand, the inclusion of flexoelectric energy term Eq. (3) also gives rise to a contribution from polarization gradients, which can be incorporated into the eigenstrain as [51],

$$\varepsilon_{ii}^{0} = Q_{iikl}P_{k}P_{l} - F_{iikl}P_{k,l},\tag{6}$$

where the first term represents the electrostrictive effect measured by Q_{ijkl} . The second term on the right-hand side of Eq. (6) describes the deformation induced by polarization gradients through the inverse flexoelectric strain coefficient $F_{ijkl} = s_{ijmn}f_{mnkl}$, where s_{ijkl} is the elastic compliance tensor. Notably, the inclusion of the flexoelectric contribution to the eigenstrain in Eq. (6) and the contribution of flexoelectric field in Eq. (4) to the driving force of polarization evolution are equivalent to the continuum-based models for flexoelectric effect in terms of higher-order stress and higher-order local electric force, respectively [52,53].

The surface energy density can be expressed as [22],

$$f_{surf} = \frac{1}{2} \left(\frac{D_1^s}{\delta_1^s} P_1^2 + \frac{D_2^s}{\delta_2^s} P_2^2 + \frac{D_3^s}{\delta_3^s} P_3^2 \right), \tag{7}$$

where δ_i^s is the extrapolation length [54] and D_i^s is the surface energy coefficient related to the gradient energy coefficient. In the presence of bulk flexoelectric effect term, i.e., Eq. (3), the polarization boundary condition at the surface of a ferroelectric thin film is modified [22,55]. In this work, we consider two types of polarization boundary condition, the Neuman boundary condition for polarization, i.e.,

$$\partial P_i/\partial z = 0, (8)$$

and the flexoelectric-modified polarization Robin boundary condition [20,22], i.e.,

$$\left. \left(\frac{D_i^s}{\delta_i^s} P_i + n_j g_{ijkl} \frac{\partial P_k}{\partial x_l} + \frac{1}{2} n_j f_{lmij} \varepsilon_{lm} \right) \right|_{h_s, h_f} = 0, \tag{9}$$

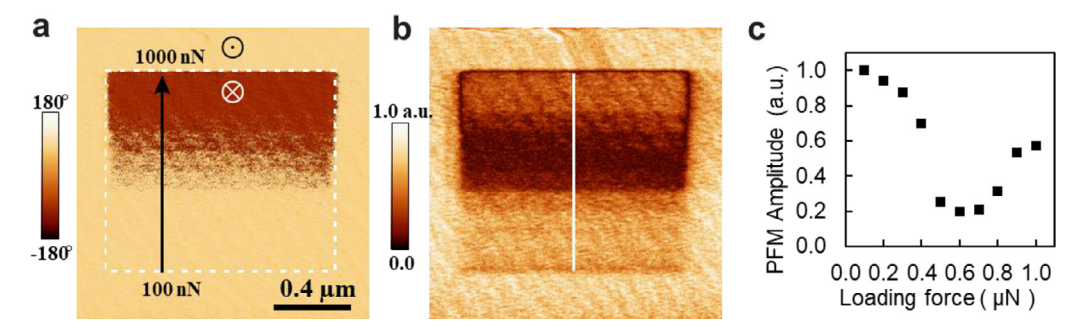


Fig. 1. Experimental measurement of the threshold loading force of mechanical switching in 5 nm BaTiO₃/La_{0.67}Sr_{0.33}MnO₃/SrTiO₃ heterostructure. PFM (a) phase and (b) amplitude images of a 1-by-1- μ m² area (denoted by the dashed frame) after tip scanning with an incremental loading force. The loading force was increasing in the bottom-up direction from 100 to 1000 nN. (c) PFM amplitude as a function of the loading force obtained by cross-section analysis along the white vertical line in (b).

for out-of-plane polarization P_3 at the film surface and the film-substrate interface. In Eq. (9), n_j the surface normal vector, g_{ijkl} the gradient energy coefficient, h_s the film-substrate interface, and h_f the film surface. The natural boundary condition corresponds to $f_{surf} = 0$, and is thus adopted for all simulation results in the Section 4 to exclude the surface effect for the convenience to discuss other influencing factors. The flexoelectric-modified boundary condition is introduced in Section 5.2 to explicitly discuss the surface effect on the thickness-dependent results of the critical force.

The Hertzian contact mechanics of a spherical indenter [56] is used to model the stress-field from the AFM tip pressing. Accordingly, the normal stress distribution on the film surface can be written as

$$\sigma_{33}^{tip}(r) = \begin{cases} -\frac{3F}{2\pi a^2} \sqrt{1 - \frac{r^2}{a^2}}, \ r \le a, \\ 0, \ r \ge a \end{cases}$$
 (10)

where r, a, and F denote the distance to the contact center, the contact radius, and the magnitude of the loading force, respectively. The contact radius a is a function of the spherical indenter radius R and the loading force F as $a = (\frac{3}{4}\frac{F}{E})^{\frac{1}{3}}$, where the effective modulus E^* is calculated from the Young's moduli and the Poisson ratios of the two contacting bodies through $\frac{1}{E^*} = \frac{1-\nu^2}{E^*} + \frac{1-\nu^2}{E^*}$. It should be noted that the analytical solution of the contact mechanic problem for a rigid sphere indenting a transversely isotropic piezoelectric half-space has been derived using the potential theory method [57] in which the surface stress distribution under zero applied electric bias reduces to Eq. (10). This stress distribution at the surface along with the coherent clamping condition of the substrate [58] are used as the mechanical boundary condition for the elastic equilibrium equation.

Eq. (1) is solved using the semi-implicit Fourier spectral scheme with periodic boundary conditions imposed on the in-plane directions of a Cartesian coordinate. The entire system is discretized by a $64\Delta x \times 64\Delta x \times 40\Delta z$ mesh where the lateral mesh size $\Delta x = 1$ nm while the out-of-plane Δz varies with film thickness. The film and substrate take up $19\Delta z$ and $13\Delta z$, respectively, along the vertical direction. Detailed descriptions of the procedure for solving the elastic and electrical equilibrium equations are provided in the previous publications [58,59]. The parameters describing the bulk free energy density, elastic and electrostrictive constants, gradient energy coefficients, and flexoelectric coefficients of BaTiO₃ are adopted from our previous works [17,60].

3. Experiments

3.1. Determination of critical force

To evaluate the minimal force to induce 180-degree polarization switching, we started from a pre-poled region with upward polarization. Mechanical writing was performed by scanning on a square region (typically $1 \times 1 \mu m^2$) via an AFM tip with incremental mechanical force from 100 nN up to 1000 nN in the slow scan direction as the scan moved forward, and the resulting domain structure was visualized by the consequent PFM scan. The PFM phase and amplitude maps for a 12-u.c.-thick BaTiO₃ film are given in Fig. 1a and 1b, respectively. Following the work by Lu et al. [16], the critical force is extracted from the corresponding force at the minimum point in the PFM amplitude versus mechanical load profile, as shown in Fig. 1c, where it reduces initially with increasing mechanical load due to the generation of antiparallel domains that are below the PFM resolution limit, and the minimum point corresponds to an equal fraction of upward and downward domains. The critical force is approximately 0.6 μ N, which agrees with the original work [16].

3.2. Effects of the AFM tip radius

Since the mechanical switching largely depends on the inhomogeneous strain within the film caused by an AFM tip pressing, the geometry of the probe tip can drastically influence the critical force. We performed mechanical writing similar to the process described in Fig. 1 with various AFM tips of tip radius ranging from \sim 9 nm to \sim 40 nm (AC240TS from Olympus, DPER18 from Mikromasch, PPP-EFM from Nanosensors, and DPE18 from Mikromasch). The PFM phase images of the switched domain using different tips are stacked in Fig. 2a. The critical forces estimated by the method discussed in Section 3.1 are plotted as a function of tip radius in Fig. 2b. It can be seen that a roughly linear relation fits well for $F_{\rm th}$ with respect to tip radius $R_{\rm tip}$.

3.3. Effects of the film thickness

The film thickness has a profound effect on the critical force required for mechanical switching, since the mechanical strain gradient generated by the AFM tip decreases rapidly along the depth of the film [16]. Here we examine the effect of BaTiO₃ film thickness ranging from 2 u.c. to 48 u.c. grown under the same conditions.

The PFM phase images after mechanical switching are stacked in Fig. 3a, and the extracted critical force dependence on film thickness is given in Fig. 3b. For ultrathin films, the critical force linearly increases from as small as 0.2 μ N in 2 u.c. to 0.6 μ N in 12 u.c. samples. However, a plateau region is observed when the BaTiO₃ thickness is above 12 u.c. to 24 u.c. where the critical force remains around 0.6 μ N. It even drops slightly to 0.5 μ N for thicker films at 48 u.c. (\sim 20 nm). However, no appreciable mechanical switching can be achieved for thicker films above 50 nm. This nontrivial thickness dependence of the critical force from experiments is puzzling because one may expect a monotonous increment in F_c with respect to the film thickness. In Section 5, we will use results from phase-field simulations to understand this unexpected trend.

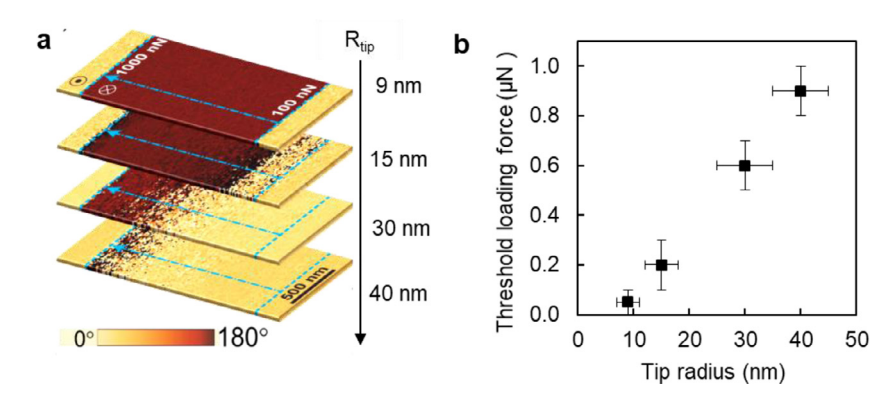


Fig. 2. Effect of AFM tip radius on mechanical switching. (a) A series of PFM phase images on 12 u.c. BaTiO₃ after mechanical writing in the center dashed area using different tips with radius around 9 nm, 15 nm, 30 nm and 40 nm respectively. (b) The threshold switching load obtained from (a) as a function of tip radius.

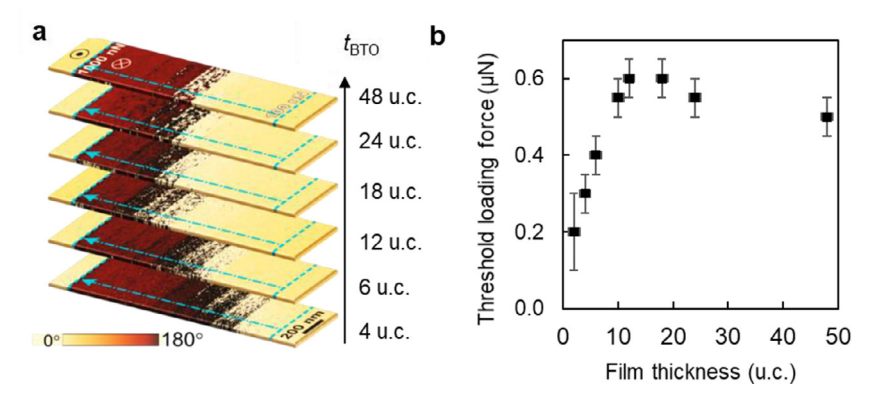


Fig. 3. Effect of film thickness on mechanical switching. (a) A series of PFM phase images after mechanical writing in the center dashed area for BaTiO₃ film thicknesses from 4 u.c. to 48 u.c. respectively. (b) The threshold switching load obtained from (a) as a function of film thickness.

3.4. Phase-field simulations

In addition to experimental measurements, we also performed three-dimensional phase-field simulations to quantify the theoretical critical force $F_{\rm c}$ in BaTiO $_3$ thin films and study the effects of the tip radius, film thickness, and misfit strain on the value of $F_{\rm c}$. In all simulations, we started from a monodomain state with upward polarization of 0.34 C/m 2 under a -2.2% biaxial misfit strain. A schematic of the simulation setup is illustrated in Fig. 4a. An incremental mechanical force F from 0 up to 6 μ N is then applied onto the film surface with a loading rate of 0.2 μ N every 2000 simulation timesteps. Afterwards, the loading force is progressively removed with the same rate, allowing the system to relax to the equilibrium state. The local polarization is approximated by averaging within a cylindrical region under the contact with a cutoff radius $r_{\rm cut}$ = 5 nm and a height equal to the film thickness. The choice of $r_{\rm cut}$ and its influence on the theoretical critical force will be discussed in detail in Section 5.

3.5. The theoretical critical force and mechanical switching dynamics

To be consistent with the experiments described in Section 3.1, we model a 5 nm (~ 12 u.c.) $BaTiO_3$ film grown on a SrTiO $_3$ substrate under a -2.2% biaxial misfit strain. The averaged local polarization as a function of the applied loading force during a loading-unloading cycle is plotted in Fig. 4b (thick red curves), from which we can identify four characteristic regimes labeled as I, II, III and IV. We also illustrated the three-dimensional distribution of the out-of-plane polarization representative of each regime in Fig. 4c. For better visualization, we only show a quarter cut of the BaTiO $_3$ film under the contact region.

Initially, when the applied force is moderate ($F < 1.2 \mu N$), the upward polarization decreases linearly, and no polarization reversal

is observed (Regime I). As the applied force increases to a critical value ($\sim 1.4 \,\mu\text{N}$), which is defined as the theoretical critical force F_{c} , the local polarization rapidly becomes negative (Regime II). Correspondingly, a cylindrical nanodomain with reversed polarization nucleates at the center of the contact region (upper panel of Fig. 4c). Note that the critical force F_c defined here is independent of the choice of the cutoff radius $r_{\rm cut}$ (discussed in Section 5.1). Further increasing the load results in a suppression of the local polarization (Regime III) and finally eliminates it (Regime IV). Regime IV suggests the entrance of a pressure-induced paraelectric state, which has also been theoretically predicted [20,61] and experimentally demonstrated [62,63]. It is also worth to note that the curve of the simulated polarization versus mechanical loads resembles that of the effective d_{33} as a function of applied forces measured by the PFM in a polycrystalline PZT sample, though the latter was captured under a much higher mechanical force (up to 25 μ N) [62]. When the applied force is progressively removed, the ferroelectricity recovers again with switched, downward polarization with a magnitude of 0.34 C/m². Therefore, the polarization-force (P-F) relation shows a hysteretic character. Unlike the P-E loop of electrically-induced switching, however, the *P-F* relation exhibits a semi-loop shape with an "open jaw," suggesting that the mechanically-induced 180-degree switching is unidirectional [16]. In other words, the polarization can only be switched from upward to downward but not the opposite. It is worth to note that there are a few recent theoretical works suggesting the possibility for switching the polarization backward by tuning the temperature and surface screening [22], which has not yet been confirmed by experiments.

The mechanism of mechanical switching of ferroelectric polarization was initially attributed to the flexoelectric effect [16,17], yet a few alternative mechanisms have also been proposed recently [20–22]. With the flexoelectric effect, the highly concentrated stress

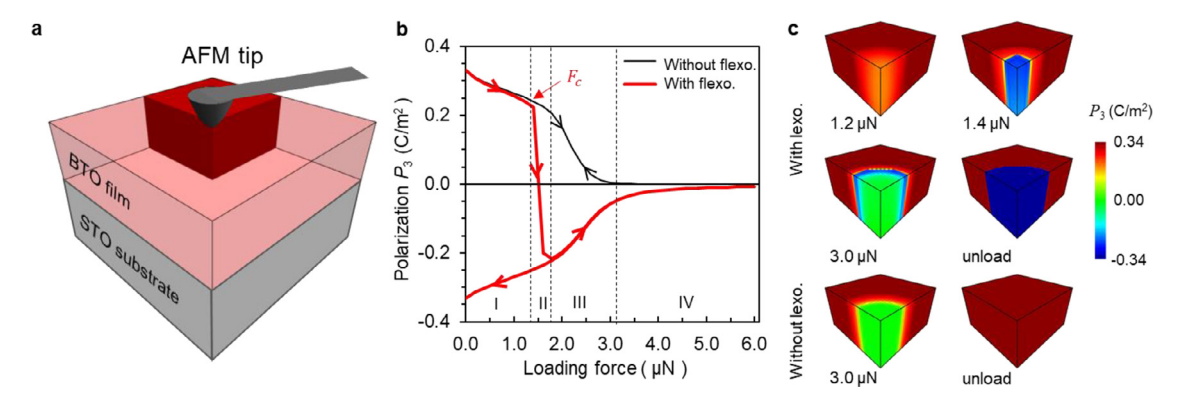


Fig. 4. Phase-field simulation of the domain evolution and polarization responses during a mechanical loading-unloading cycle. (a) A schematic of the initial setup of the phase-field model. A quarter cut of the BaTiO₃ film is highlighted in red to denote the regions for visualizing the polarization distribution in (c). (b) Local polarization as a function of the loading force during the loading-unloading process, with (thick red curve) and without (thin black curve) considering the flexoelectric contribution. The arrowheads along the two curves indicate the loading-unloading directions during a cycle. The red arrow denotes the theoretical critical force F_c . (c) 3D distributions of out-of-plane polarization in the BaTiO₃ film under different mechanical loading forces or after unloading, with (upper panel) and without (lower panel) considering the flexoelectric contribution. The film thickness is 12 u.c., the tip radius is 86 nm, and the misfit strain is -2.2%. (For interpretation of the references to colour in this figure legend, the reader is referred to the web version of this article.)

field created by the tip pressing is equivalent to a local electric field, known as the flexoelectric field E^{flexo} , which could reach as high as 10^8 V/m. Once the local E^{flexo} exceeds the coercive field of ferroelectricity, polarization reverses. However, under such a high mechanical pressure, the piezoelectric effect on the polarization is also significant. To distinguish the role of flexoelectricity from piezoelectricity. we repeated the same simulation procedure while artificially "turning off" the flexoelectric contribution by setting all flexocoupling coefficients to zero. In this sense, one can isolate the piezoelectric contribution to the change of polarization [17]. The resulting P-F relation without considering the flexoelectric effect is plotted in Fig. 4b with thin black curves. When the force is small, a linear reduction of polarization is observed, which almost overlaps with the case considering flexoelectricity, which suggests the dominance of piezoelectric contribution in Regime I. Keeping increasing the load, however, does not lead to a polarization reversal, but ending up with a more rapid drop of polarization magnitude (Regime III) and an earlier entrance into the paraelectric state (Regime IV). Upon unloading, the system recovers its the pristine state, as shown in the lower panel of Fig. 4c, revealing the essential role of flexoelectricity in realizing the mechanical switching.

We further examined the radius of the switched nanodomain, R_{SWL} , and the out-of-plane flexoelectric fields, E_3^{flexo} , as a function of the loading force F in Fig. 5. The force dependence of the local E_3^{flexo} (averaged within the same region as the local polarization) peaks at F

 $\sim 0.4~\mu N$, reaching as large as $\sim 8~MV/m$. We define the force at which E_3^{flexo} reaches the maxima as $F_{\rm m}$, which reflects the tunability of the mechanical switching. It is interesting to see that $F_{\rm m}$ is not identical to $F_{\rm c}$, which suggests the effect of piezoelectricity on modifying the barrier of polarization switching. E_3^{flexo} quickly drops with further increase in the loading force. This can be understood by examining the E_3^{flexo} distribution under the contact area for $F=1.4~\mu N$ and $F=4.0~\mu N$, as shown in Fig. 5b. In both cases, the negative E_3^{flexo} is concentrated near the film bottom while near zero close to the film surface. The weakening of E_3^{flexo} adjacent to the surface becomes more striking under higher loading forces, which explains why E_3^{flexo} peaks at a relatively low mechanical load.

From the force dependence of the radius of the switched domain, $R_{\rm Swt}$, one can identify the minimal force responsible for the nucleation of domain switching, i.e., the theoretical critical force, to be $F_{\rm c}=1.4~\mu{\rm N}$. Note that $F_{\rm c}$ defined here agrees with the one defined by the turning point from Regime I to Regime II in Fig. 4a, suggesting the self-consistency of these two approaches. It is worth to note that the area of switched domains ($\sim R_{\rm swt}^2$) remains to be smaller than the contact area ($\sim R_{\rm con}^2$) during the entire loading process, indicating that the mechanically-switched domain is always laterally confined. This spatial confinement of mechanically-written nanodomains has also been observed in several experiments [16,41], which contrasts to the electrically-written domain that grows laterally with longer pulse time [64]. This unique feature of mechanical

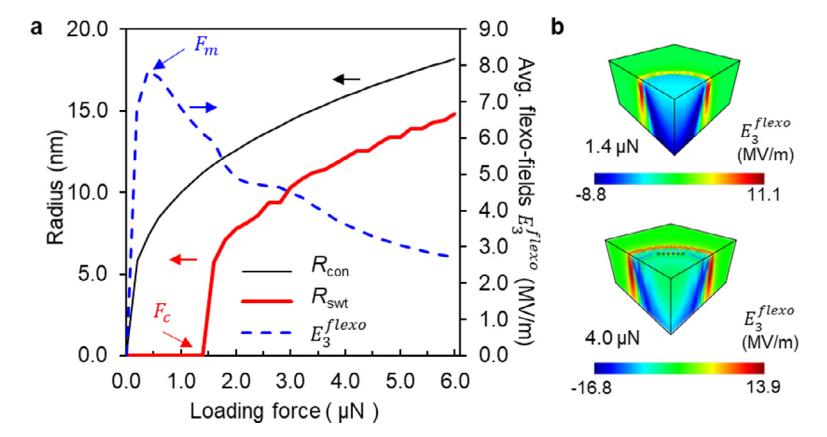


Fig. 5. Results from phase-field simulations of switched domain size and flexoelectric field as a function of the loading force during a mechanical loading process. (a) The contact radius R_{con} (thin black solid curve), switched domain radius R_{swt} (red solid curve), and locally averaged out-of-plane flexoelectric field E_3^{flexo} (blue dashed curve) as a function of the loading force. Note that the absolute values of the negative flexoelectric field are used for plotting. F_m stands for the force at which the flexoelectric field peaks and F_c the critical force of polarization switching. (b) 3D distributions of the out-of-plane flexoelectric field under 1.4 and 4.0 μ N loading forces. The film thickness, tip radius, and misfit strain for the simulation are identical to those in Fig. 4. (For interpretation of the references to colour in this figure legend, the reader is referred to the web version of this article.)

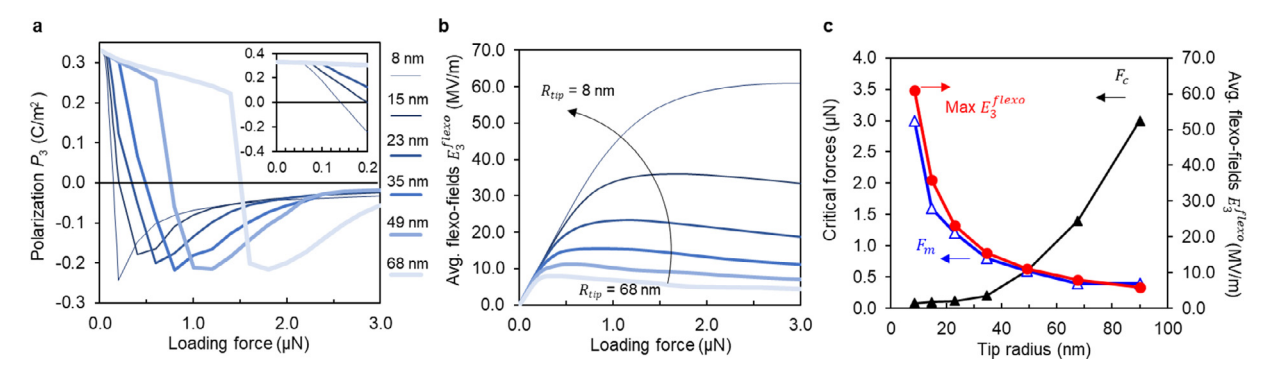


Fig. 6. Results from phase-field simulations of the effect of AFM tip radius on the critical force of mechanical switching. (a) Locally averaged polarization as a function of the loading force during the loading process using different tip radius. The inset magnifies the low-force region. (b) Locally averaged out-of-plane flexoelectric fields E_3^{flexo} as a function of the loading force using different tip radius. The legend is the same as in (a). Note that the absolute values of the negative flexoelectric field are used for plotting. (c) The critical force F_c (solid black triangles), the maximal averaged flexoelectric field E_3^{flexo} (solid red circles) and corresponding force F_m (blank blue triangles) as functions of the tip radius. The solid lines are guides to eyes. In all these simulations, the film thickness is 12 u.c., and the misfit strain is -2.2%. (For interpretation of the references to colour in this figure legend, the reader is referred to the web version of this article.)

switching is beneficial to the ultrahigh-density data storage and the nanoscale engineering of ferroelectric domain and domain walls [16,26,34].

3.6. Effects of the AFM tip radius

We further studied the dependence of the critical force $F_{\rm c}$ on the tip radius $R_{\rm tip}$ using the same setup as described in 4.1 while varying the radius of the spherical indenter of the Hertzian contact model. The P-F force curves with $R_{\rm tip}$ = 8 - 68 nm were calculated and plotted in Fig. 6a, from which $F_{\rm c}$ can be extracted. The force dependences of $E_3^{\rm flexo}$ for each case are presented in Fig. 6b from which the force $F_{\rm m}$ corresponding to maximal $E_3^{\rm flexo}$ can be identified. The tip radius effect on $F_{\rm c}$, $F_{\rm m}$, and maximal $E_3^{\rm flexo}$ are summarized in Fig. 6c.

As shown in Fig. 6a, a linear drop of polarization at a low applied force (Regime I) occurs with a similar slope independent of the tip radius. The effect of the tip radius is reflected by the fact that the increase of F_c as the tip becomes blunter, which qualitatively agrees with the experiments (c.f. Section 3.2). In all cases, the window of Regime II is narrow (0.2 \sim 0.4 μ N), suggesting that the mechanical switching occurs abruptly as long as the load exceeds F_c . Nevertheless, the Regime III becomes wider for a sharper tip, as manifested by the longer "tail" in the P-F curve. This elongation of Regime III can be understood by examining the force dependence of the E_3^{flexo} in Fig. 6b. For a very sharp tip, e.g., $R_{\rm tip}$ = 8 nm, E_3^{flexo} keeps growing up to a relatively high force, e.g., $F_{\rm m}$ = 3.0 μ N; therefore, a downward polarization remains. Fig. 6c also demonstrates that E_3^{flexo} and the force $F_{\rm m}$ are sensitive to the choice of tip radius, indicating an

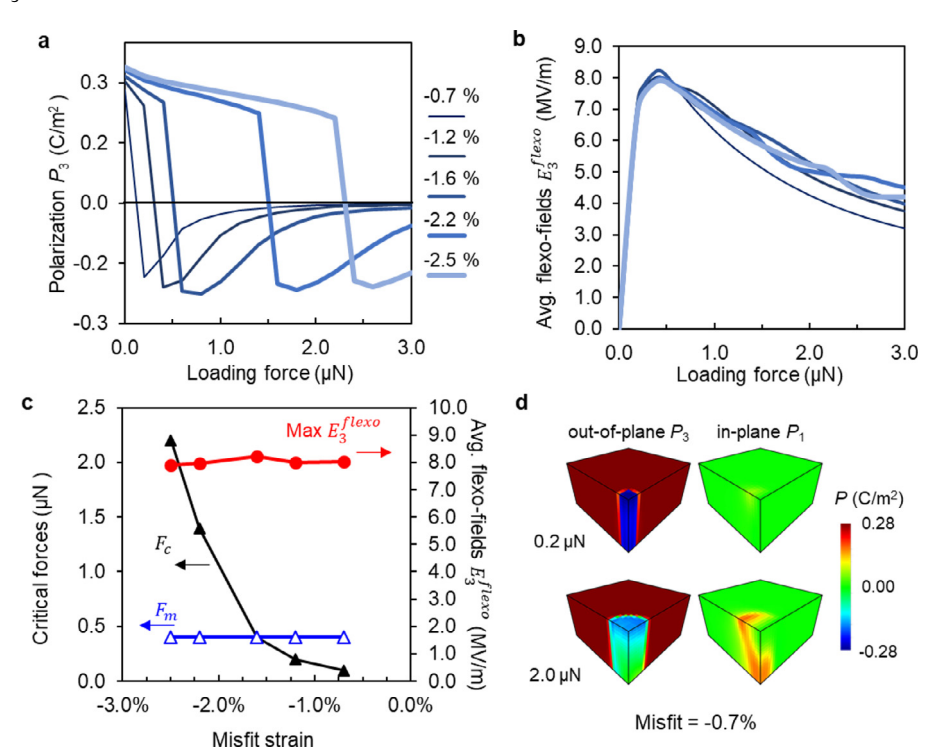


Fig. 7. Results from phase-field simulations of the effect of the biaxial misfit strain of the substrate on the critical force of mechanical switching. (a) Locally averaged polarization as a function of loading force during the loading process with different misfit strains. (b) Locally averaged out-of-plane flexoelectric fields E_3^{flexo} as a function of loading force with different misfit strains. The legend is the same as in (a). Note that the absolute values of the negative flexoelectric field are used for plotting. (c) The critical force F_c (solid black triangles), the maximal averaged flexoelectric field E_3^{flexo} (solid red circles) and corresponding force F_m (blank blue triangles) as functions of the tip radius. The solid lines are guide to eyes. In all these simulations, the film thickness is 12 u.c., and the tip radius is 68 nm. (For interpretation of the references to colour in this figure legend, the reader is referred to the web version of this article.)

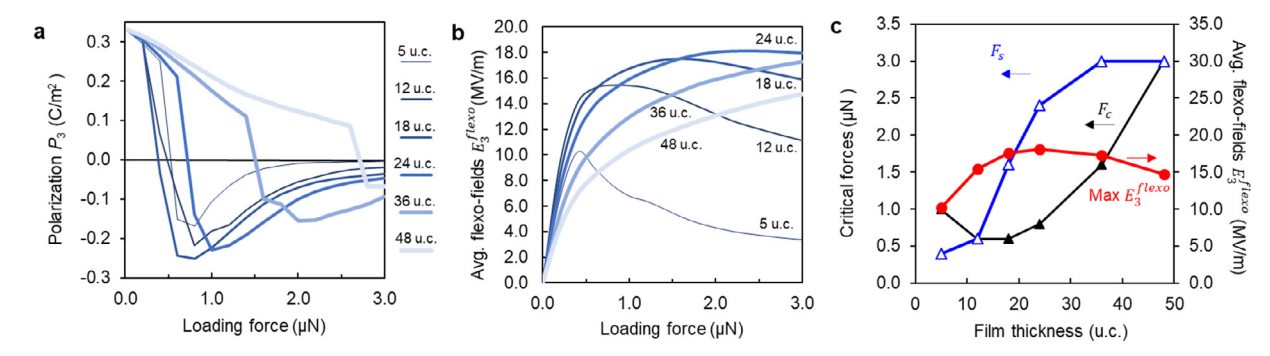


Fig. 8. Phase-field simulation of the effect of the film thickness on the critical force of mechanical switching. (a) Locally averaged polarization as a function of loading force during the loading process in films with different thicknesses. (b) Locally averaged out-of-plane flexoelectric fields E_3^{flexo} as a function of loading force in films with different thicknesses. The legend is the same as in (a). Note that the absolute values of the negative flexoelectric field are used for plotting. (c) The critical force F_c (solid black triangles), the maximal averaged flexoelectric field E_3^{flexo} (solid red circles) and corresponding force F_m (blank blue triangles) as functions of the tip radius. The solid lines are guides to eyes. In all these simulations, the misfit strain is -2.2%, and the tip radius is 49 nm. (For interpretation of the references to colour in this figure legend, the reader is referred to the web version of this article.)

enhanced tunability of the mechanical switching by using a sharper tip.

Fig. 6c shows that F_c increases linearly with the $R_{\rm tip}$ when $R_{\rm tip}$ is less than \sim 40 nm, which is consistent with our experimental results in Fig. 2b. When the tip radius further enlarges, the critical forces grows quadratically, making the mechanical switching more difficult. This finding explains the worn-out of an AFM tip in experiments, i.e., it becomes harder to achieve mechanical switching after numerous times of usage [16]. Therefore, the blunting of probe tips after repetitive scanning is another challenge to overcome for realizing a robust mechanical control of ferroelectricity at the nanoscale.

3.7. Effects of the misfit strain

Next, we examined the misfit strain effect on the mechanical switching by using the 5 nm $BaTiO_3$ thin film and $R_{tip} = 68$ nm while varying the biaxial misfit strain. The *P-F* and E_3^{flexo} -*F* curves under various misfit strains are plotted in Fig. 7a and 7b, respectively, and the extracted values, i.e., F_c , F_m , and maximal E_3^{flexo} , as a function of the misfit strain are shown in Fig. 7c. One can see Regime I becomes narrower and the linear drop of polarization becomes stiffer as the misfit strain is less compressive, indicating that the out-of-plane polarization become "softer" and more susceptible to be influenced by the mechanical stress. An extreme is the case with -0.7% misfit strain in which the Regime I disappears, and the local polarization directly drops to a negative value upon a 0.2 μ N load. On the other hand, the misfit strain tends to have negligible influence on the flexoelectric field, as shown in Fig. 7b and 7c, which suggests that the decline of F_c is due to the lowering of the intrinsic switching barriers rather than the enlargement of the driving force E_3^{flexo} . This finding supports a simple thermodynamic analysis in a previous work [30]. However, unlike the experimental results of Ref. [30], the simulated dependence of F_c on the misfit strain shown here is nonlinear. One possible reason may be due to the choice of tip radius which can significantly affects F_c , which was unfortunately not reported in Ref. [30] and could hardly be kept constant in practice.

The effect of the misfit strain on F_c has been experimentally studied in BaTiO₃ [30] and PbZr_{0.2}Ti_{0.8}O₃ [33] thin films. However, when the compressive epitaxial strain becomes relatively small, other domain variants with in-plane polarization may appear under a mechanical pressure [61,65], which has not been captured by previous experiments [30, 33] or theoretical studies [20]. To gain some insights on this issue, we plotted the 3D distributions of the in-plane polarization P_1 and the out-of-plane polarization P_3 under 0.2 μ N and 2.0 μ N loads in Fig. 7d for the case when the misfit strain is -0.7%. With a small loading force (0.2 μ N), only 180-degree switching of P_3 is observed. However, when the force is large (2.0 μ N), significant P_1 appears (\sim 0.3 C/m²) and forms a nanosized domain under

the contact whereas P_3 is negligible. In other words, the increment of the load does not lead to a paraelectric state, as for the case with -2.2% misfit strain (Fig. 4c); instead, a 90-degree ferroelastic switching is induced. This in-plane polar domain is unstable after unloading due to the large biaxial compressive misfit strain. Nevertheless, it is interesting to test whether a 90-degree domain switching can be mechanically induced by AFM tip scanning in systems where a/c ferroelastic domains are metastable, such as $Pb(Zr_{0.2}Ti_{0.8})O_3$ thin films [66]. Furthermore, the finding also emphasizes that although reducing the substrate clamping can reduce F_c , it may also result in other domain variants with in-plane polarization, which may cause fatigue or retention problems [66]. Very recently, it is predicted that a vortex polar state can be created by mechanical pressing in BaTiO₃ thin films subject to a reduced misfit strain [67].

3.8. Effects of the film thickness

We finally turned to examine the film thickness effect on the critical force F_c . The film thickness varies from 5 u.c. up to 48 u.c. (\sim 2 – 19 nm) while the misfit strain is maintained to be -2.2% and the $R_{\rm tip}$ = 49 nm to ease the mechanical switching. The force-dependent results are summarized in Fig. 8a and 8b, and the extracted quantities $(F_{\rm c}, F_{\rm m}, {\rm maximal}\ E_3^{flexo})$ are plotted against the film thickness in Fig. 8c. In all cases, the P-F relations exhibit four characteristic regimes as discussed in previous sections but the shape of P-F curves changes with respect to the film thickness in a nontrivial way. F_c does not monotonically decrease as the film becomes thinner, as it may be intuitively suggested. Instead, the relation is parabolic: F_c decreases from 3.0 μ N to 0.6 μ N for films with a thickness of 48 u.c. to 12 u.c., but it increases again when the film becomes ultrathin (= 5 u.c.). In parallel, the peak value of E_3^{flexo} is also suppressed for the 5 u.c. ultrathin film as well as for thicker films (> 24 u.c.) (Fig. 8c). Besides, an enhanced tunability of E_3^{flexo} is reflected by the increase of F_m . A more in-depth discussion on these nonintuitive behaviors will be given in the next section.

4. Discussion

The phase-field simulation results presented in Section 4 agree with our experimental results presented in Section 3 and with those from some previous works [30,33] in the following several aspects. First, the shape of the simulated P-F semi-loop in Fig. 4a resembles the PFM amplitude-force profile in Fig. 1c, considering that the PFM amplitude is approximately proportional to the polarization magnitude. Second, both our experiments and simulations show that the critical force F_c is significantly reduced by using a sharper tip. Third, the simulation results on the misfit effect agree qualitatively well with the previous experiments [30,33], which reveals that the critical

force decreases with the relaxing of compressive substrate constraints due to the lowering of the intrinsic switching barrier. Nevertheless, there are several discrepancies and ambiguities worth further discussions. For example, $F_{\rm c}$ estimated in experiments is $\sim 0.6~\mu$ N whereas the simulated value is $\sim 1.4~\mu$ N. Moreover, our experiments suggest a linear increase followed by a plateau region in the film thickness dependence of $F_{\rm c}$, whereas the simulation predicts a parabolic dependence of $F_{\rm c}$ on film thicknesses. In this section, we address the possible reasons for these issues.

4.1. Ambiguities in determining the critical force

There are several possible reasons for the deviations in quantifying the critical force F_c from experiments and simulations. First, the loading mode of the AFM tip is different. In the experiment, the AFM tip is operating in a scanning mode with an incremental force along the slow scan direction [16,30,33]. In the simulations, however, the tip position is kept fixed at the same position while the loading force is ascending and then descending. As shown by several works [20,28,44] the stress gradient can be enhanced when the tip is scanning, thereby lowering F_c . Second, the definition of F_c differs. In experiments, the critical force corresponds to the dip in the PFM amplitude-force plot, corresponding to a state where 50% of the local polarization is switched [16]. By contrast, in simulations, the turning point which separates the linear regime (Regime I) and the switching regime (Regime II) is taken as the critical force (Fig. 4b), representing the onset of the reversed domain nucleation. Third, although the PFM amplitude is proportional to the local polarization magnitude, it also depends on the lateral and vertical resolution of the PFM response [68]. Likewise, the simulated P-F curve also depends on the shape and size of the region for averaging the polarization. In the present work, we averaged the polarization within a cylindrical region under the contact area with a fixed cutoff radius r_{cut} = 5 nm and a height equal to the film thickness. The choice of $r_{\rm cut}$ affects the shape of the P-F semi-loops, as illustrated in Fig. 9. If we define F_c as the crossing point of the *P-F* curve with the x-axis (labeled by $F_{P=0}$), similar to that defined in experiments (Fig. 1), then F_c will depend on r_{cut} . In contrast, if we use the force for switched domain nucleation (labeled by $F_{\rm nuc}$) as $F_{\rm c}$, it does not depend on the choice of $r_{\rm cut}$. Note that, $F_{P=0}$ converges to F_{nuc} for smaller r_{cut} , as shown in the inset of Fig. 9. Considering this issue, we use the nucleation force F_{nuc} to represent the theoretical critical force F_c throughout the paper.

It is also worth to note that several factors that present in experiments were neglected in the present simulation. For example, the presence of point defects such as oxygen vacancies can facilitate polarization switching by providing nucleation sites [69], which is not considered in the present model. Moreover, the scanning of an AFM tip on the film surface may change the surface charge screening [70] and induce polarization switching by electrochemical processes rather than by the flexoelectric effect. This issue has been comprehensively discussed in a recent review article [71] and theoretically by Cao et al. [21].

4.2. The thickness dependence of critical forces

To understand the counterintuitive thickness dependence of $F_{\rm c}$ shown in Section 4.4, we plotted the 3D distribution of $E_3^{{\rm flexo}}$ for different film thicknesses at their peak values, as illustrated in Fig. 10a. For ultrathin films (5 u.c.), there is a "hollow" region under the contact area in which $E_3^{{\rm flexo}}$ is weakened. This finding is understandable because for ultrathin films against the tip pressing, the stress field can penetrate through the whole film without much decay, thereby generating a negligible stress gradient across the film (Fig. 10a). For thicker films (e.g., ≥ 24 u.c.), most of the region under the tip contact is covered by a large negative $E_3^{{\rm flexo}}$. When the film is even thicker (e.g., 48 u.c.), the negative $E_3^{{\rm flexo}}$ can fully develop into the film, penetrate

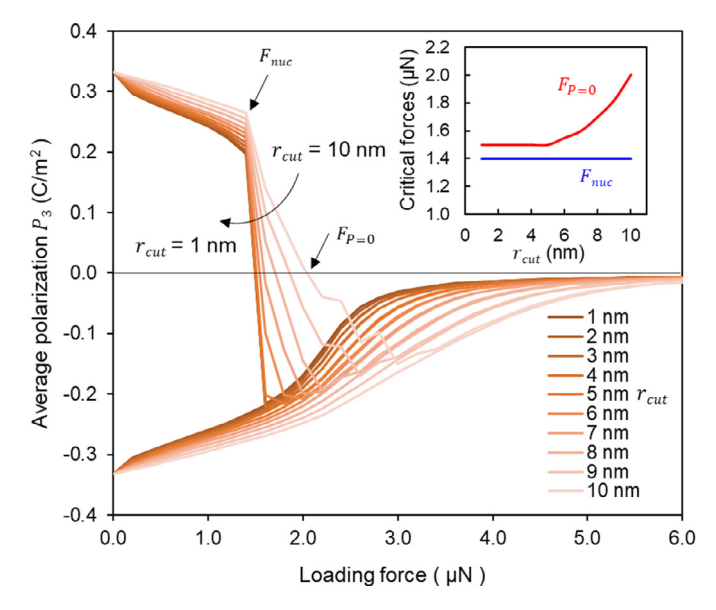


Fig. 9. Different definitions of the critical force from phase-field simulation results and the choice of the cutoff radius r_{cut} for averaging the local polarization. The inset shows the dependence of F_{nuc} and $F_{P=0}$ on the cutoff radius r_{cut} . The definitions of these symbols are provided in text.

a certain distance, and then decay exponentially until reaching the film-substrate interface. A more quantitative comparison is given in Fig. 10b where the in-depth profiles of E_3^{flexo} under F = 3.0 μ N are compared for different film thicknesses. It is shown that the penetration depth of E_3^{flexo} (when E_3^{flexo} reaches maxima) is no more than \sim 7 nm for all cases studied. In this sense, the simulation results indicate that the flexoelectric field *alone does not* account for the mechanical switching in ultrathin or relatively thick films.

In the experiments, the mechanical switching is rather straightforward in ultrathin films (5 u.c.) even with a mechanical load of $\sim\!0.2~\mu\text{N}.$ Moreover, a plateau regime is seen from 12 u.c. to 48 u.c. where the critical force ceases to increase with the film thickness. To understand the discrepancy between experimental and simulation results, we discuss two plausible mechanisms, namely, the misfit strain relaxation in thicker films and the surface effect due to polarization relaxation.

In epitaxial thin films, strain relaxation occurs when the film exceeds a critical thickness. The strain relaxation can be achieved through the formation of interfacial dislocations or the presence of oxygen vacancies [72]. A classical model to account for the strain relaxation in thin films was proposed by People and Bean [73], which has been successfully applied to perovskite ferroelectric thin films [74,75]. The model assumes that the effective relaxed misfit strain is uniform across the film thickness and can be calculated by

$$\varepsilon(h) = 1 - \frac{1 - \varepsilon_0}{1 - \varepsilon_0 \left(1 - \frac{h_c}{h}\right)},\tag{11}$$

where h is the film thickness, h_c is the critical thickness for strain relaxation, and ε_0 is the nominal misfit strain without relaxation. The critical thickness h_c was reported to be 5 - 7 nm for BaTiO₃ grown on SrTiO₃ substrates [76-78]. Here, we adopt h_c = 6.7 nm [78], which reasonably agrees with the theoretical value (9.8 nm) calculated based on the People-Bean model. As a result, the 18 u.c., 24 u.c., 36 u.c., and 48 u.c. films all suffer from misfit strain relaxation to some extent.

The effective misfit strain as a function of film thickness after considering the relaxation effect is shown in Fig. 11a as calculated by Eq. (11). We repeated the same simulation procedure in Section 4.4 while using the relaxed misfit strains. The newly extracted critical force against the film thickness is shown in Fig. 11b. The experimental results in Fig. 3b and simulation results without considering the

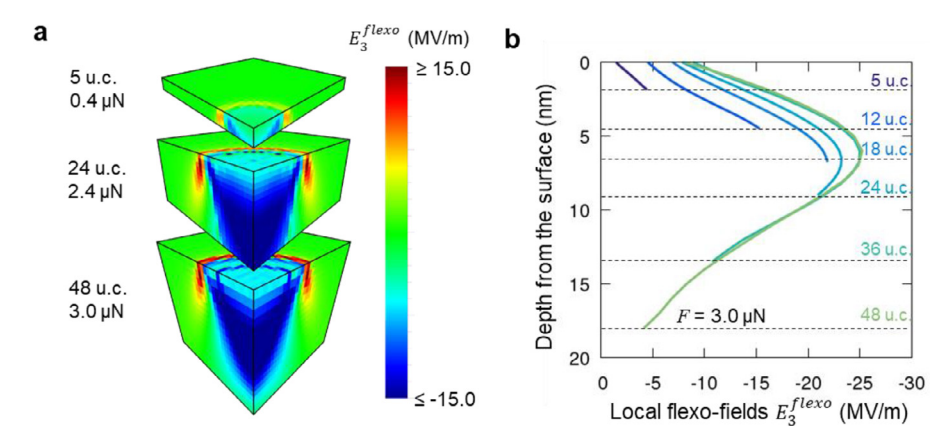


Fig. 10. Results from phase-field simulations of the effect of film thickness on the distribution of flexoelectric fields. (a) 3D distributions of the out-of-plane flexoelectric field under 3.0 μ N loading force in films with different thickness. (b) Vertical profiles of the local flexoelectric fields at the contact center from the film surface to bottom for different film thickness under 3.0 μ N loading force. The misfit strain is -2.2%, and the tip radius is 49 nm.

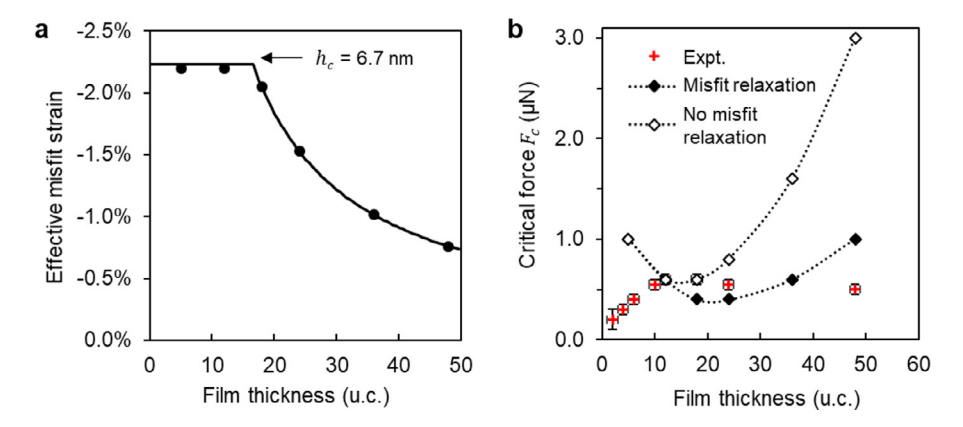


Fig. 11. Results from phase-field simulations of the effect of misfit strain relaxation on the critical force of mechanical switching. (a) Effective misfit strain as a function of film thickness calculated by the PB model using a critical thickness h_c = 6.7 nm, as indicated by the black arrow. (b) The critical force F_c as a function of film thickness with (solid black diamonds) and without (blank black diamonds) considering the misfit relaxation. The experimental results in Fig. 3 are replotted for comparison. The dashed lines are guides to eyes.

misfit relaxation in Fig. 8c are replotted for comparison. One can see that F_c decreases when considering the misfit relaxation effect, leading to a plateau region for 18-24 u.c. cases. Nevertheless, the critical force rises again for thicker films (>24 u.c.).

Another mechanism is the polarization relaxation at the surface, which is known to be significant when the film thickness is of a few nanometers [79]. With the presence of bulk flexoelectric effect, the polarization relaxation is described by the boundary condition given in Eq. (9). The equilibrium polarization profiles across the film thickness for a single domain are obtained and shown in Fig. 12a, Considerable decrease of polarization magnitude near the film surface and bottom suggests a strong surface effect on the polarization, which lowers the average polarization in the film and makes it more vulnerable to be switched. We perform the thickness-dependent simulations with the surface effect considered and plot the results in Fig. 12b in comparison with the results without surface effect and the experimental measurements. The critical force F_c is significantly reduced due to the consideration of the surface polarization relaxation. In particular, F_c for ultrathin films (5 u.c.) reduces from 1.0 μ N to 0.1 μ N. A plateau region of F_c (= 0.6 μ N) appears for film thickness from 12 u.c. to 36 u. c., although an increase of F_c to 0.8 μ N remains for thicker (48 u.c.) films. Apparently, the surface effect can facilitate mechanical switching not only for ultrathin films but also for thicker films due to the softening of polarization at the boundaries. Therefore, the discrepancy of the thickness-dependence of F_c from experimental measurement and simulations can be accounted for by incorporating the surface effect through flexoelectric-mediated polarization relaxation.

Finally, it is worth noting that mechanical switching has been reported in relatively thick perovskite films (80 - 100 nm) in many recent works [28,34,80], which cannot be simply explained by the flexoelectric mechanism. Here, we briefly comment on this issue. First, it remains controversial whether the observed change of PFM images after a mechanical tip scanning is indeed due to polarization switching [71]. Second, even if the domain has been reversed, the mechanism is not necessarily to be relevant to the flexoelectric effect, as suggested in some recent theoretical works [20-22]. Other possible mechanisms such as the bulk transport of charged point defects [21], surface electrochemical effects [21,22,81], and shear stresses [28,45,82], may also account for the mechanical switching in relatively thick films. Nevertheless, few of these works investigated the mechanical switching in films thicker than 20 nm. Therefore, for future works, it is crucial to perform in situ observation of mechanical switching by using high-resolution electron microscopy [83,84] and explore other mechanisms beyond the present ones for fundamentally understanding the mechanical switching in thick films.

5. Summary

In this work, we systematically investigated the critical force of mechanically induced polarization switching by an AFM tip in $BaTiO_3$ ferroelectric thin films using AFM-based experiments and phase-field simulations. Both experiments and simulations demonstrate that the AFM tip radius, the film thickness, and the epitaxial misfit strain have impacts on the value of the critical force. In particular, the critical

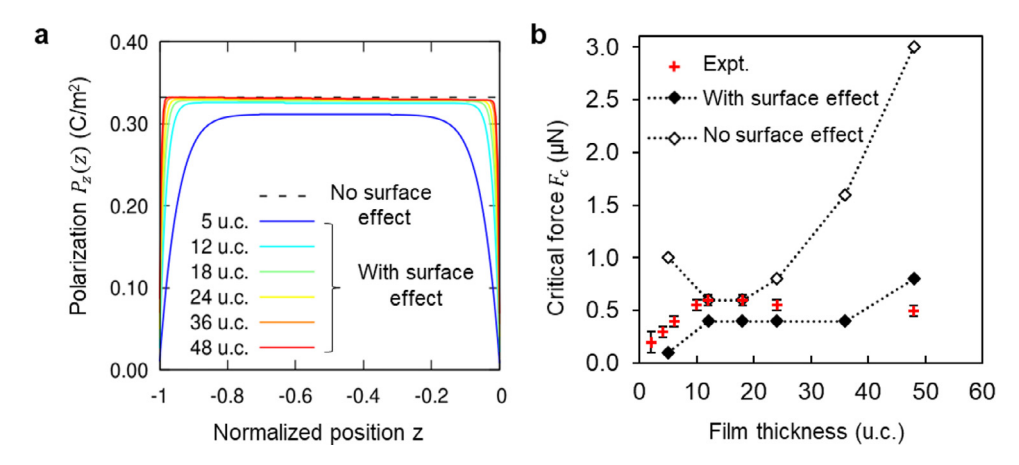


Fig. 12. Results from phase-field simulations of the surface effect due to polarization relaxation on the critical force of mechanical switching. (a) Equilibrium polarization distribution $P_3(z)$ across the films with various thicknesses before mechanical loading. The dashed line is calculated by using the free boundary condition whereas the rests are calculated by using the flexoelectric-modified boundary condition for polarization. (b) The critical force F_c as a function of film thickness with (solid black diamonds) and without (empty black diamonds) considering the surface effect. In (b), the experimental results in Fig. 3 are replotted for comparison. The dashed curves are guides to eyes.

force can be reduced by using a sharper tip or by decreasing the substrate constraint. The film thickness effect is counterintuitive perhaps due to the misfit relaxation, the polarization relaxation near surfaces and the involvement of alternative mechanisms other than the flexoelectric effect. The simulations also reveal an interplay of flexoelectric and piezoelectric effects during a loading-unloading cycle by tracking the change of polarization and flexoelectric field distributions. The understanding of mechanical switching of ferroelectric polarization at the nanoscale obtained in this work will be useful for providing guidance to explore the mechanical control of ferroelectrics-based nanodevices.

Declaration of competing interest

The authors declare that they have no known competing financial interests or personal relationships that could have appeared to influence the work reported in this paper.

Acknowledgments

This work at The Pennsylvania State University is supported by the US National Science Foundation through Grant No. DMR-1744213 (L.-Q.C. and B.W.) and through (NSF)-Materials Research Science and Engineering Center (MRSEC) grant number DMR-1420620 (B.W.). The work at the University of Nebraska-Lincoln was supported by the US National Science Foundation through the MRSEC under Grant No.DMR-1420645 (PFM experiments) and by the U.S. Department of Energy, Office of Science, Basic Energy Sciences, Division of Materials Sciences and Engineering, under Award No. DE-SC0004876 (fabrication of thin films). The work at University of Wisconsin-Madison is supported by the Army Research Office through grant W911NF-17-1-0462. B. W. appreciates the reading and comments of the manuscript by Dr. Jianjun Wang and Xiaoxing Cheng.

References

- [1] J.F. Scott, Ferroelectric Memories, Springer Science & Business Media, 2013.
- [2] K. Uchino, Ferroelectric Devices, CRC press, 2018.
- [3] B.W. Wessels, Ferroelectric epitaxial thin films for integrated optics, Annu. Rev. Mater. Res. 37 (2007) 659–679, doi: 10.1146/annurev.matsci.37.052506.084226.
- [4] A. Gruverman, O. Auciello, H. Tokumoto, Imaging and control of domain structures in ferroelectric thin films via scanning force microscopy, Annu. Rev. Mater. Sci. 28 (1998) 101–123, doi: 10.1146/annurev.matsci.28.1.101.
- [5] G. Zavala, J.H. Fendler, S. Trolier-McKinstry, Characterization of ferroelectric lead zirconate titanate films by scanning force microscopy, J. Appl. Phys. 81 (1997) 7480–7491, doi: 10.1063/1.365350.

- [6] D.A. Bonnell, S.V. Kalinin, A.L. Kholkin, A. Gruverman, Piezoresponse Force Microscopy, A Window into Electromechanical Behavior at the Nanoscale, MRS Bull. 34 (2009) 648–657, doi: 10.1557/mrs2009.176.
- [7] S.V. Kalinin, B.J. Rodriguez, S. Jesse, Y.H. Chu, T. Zhao, R. Ramesh, S. Choudhury, L.Q. Chen, E.A. Eliseev, A.N. Morozovska, Intrinsic single-domain switching in ferroelectric materials on a nearly ideal surface, Proc. Natl. Acad. Sci. 104 (2007) 20204–20209, doi: 10.1073/pnas.0709316104.
- [8] C.T. Nelson, P. Gao, J.R. Jokisaari, C. Heikes, C. Adamo, A. Melville, S.H. Baek, C.M. Folkman, B. Winchester, Y. Gu, Y. Liu, K. Zhang, E. Wang, J. Li, L.Q. Chen, C.B. Eom, D.G. Schlom, X. Pan, Domain dynamics during ferroelectric switching, Science 334 (80) (2011) 968–971, doi: 10.1126/science.1206980.
- [9] D. Li, D.A. Bonnell, Controlled patterning of ferroelectric domains: fundamental concepts and applications, Annu. Rev. Mater. Res 38 (2008) 351–368, doi: 10.1146/annurev.matsci.37.052506.084303.
- [10] L. Keeney, T. Maity, M. Schmidt, A. Amann, N. Deepak, N. Petkov, S. Roy, M.E. Pemble, R.W. Whatmore, Magnetic field-induced ferroelectric switching in multiferroic aurivillius phase thin films at room temperature, J. Am. Ceram. Soc. 96 (2013) 2339–2357, doi: 10.1111/jace.12467.
- [11] T. Kimura, T. Goto, H. Shintani, K. Ishizaka, T. Arima, Y. Tokura, Magnetic control of ferroelectric polarization, Nature 426 (2003) 55–58, doi: 10.1038/nature02018.
- [12] D.M. Evans, A. Schilling, A. Kumar, D. Sanchez, N. Ortega, M. Arredondo, R.S. Katiyar, J.M. Gregg, J.F. Scott, Magnetic switching of ferroelectric domains at room temperature in multiferroic PZTFT, Nat. Commun. 4 (2013) 1534, doi: 10.1038/ncomms2548.
- [13] R.V. Wang, D.D. Fong, F. Jiang, M.J. Highland, P.H. Fuoss, C. Thompson, A.M. Kolpak, J.A. Eastman, S.K. Streiffer, A.M. Rappe, G.B. Stephenson, Reversible chemical switching of a ferroelectric film, Phys. Rev. Lett. 102 (2009) 047601, doi: 10.1103/PhysRevLett.102.047601.
- [14] Y. Kim, İ. Vrejoiu, D. Hesse, M. Alexe, Reversible plasma switching in epitaxial BiFeO₃ thin films, Appl. Phys. Lett. 96 (2010) 16–18, doi: 10.1063/1.3431585.
- [15] Y. Tian, L. Wei, Q. Zhang, H. Huang, Y. Zhang, H. Zhou, F. Ma, L. Gu, S. Meng, L.Q. Chen, C.W. Nan, J. Zhang, Water printing of ferroelectric polarization, Nat. Commun 9 (2018) 3809, doi: 10.1038/s41467-018-06369-w.
- [16] H. Lu, C.W. Bark, D. Esque De Los Ojos, J. Alcala, C.B. Eom, G. Catalan, A. Gruverman, Mechanical writing of ferroelectric polarization, Science 335 (80) (2012) 59–61, doi: 10.1126/science.1218693.
- [17] Y. Gu, Z. Hong, J. Britson, L.Q. Chen, Nanoscale mechanical switching of ferroelectric polarization via flexoelectricity, Appl. Phys. Lett. 106 (2015) 022904, doi: 10.1063/1.4905837.
- [18] P. Zubko, G. Catalan, A.K. Tagantsev, Flexoelectric Effect in Solids, in: DR Clarke (Ed.), Annual Review of Materials Research, 2013, pp. 387–421, doi: 10.1146/annurev-matsci-071312-121634.
- [19] B. Wang, Y. Gu, S. Zhang, L.-Q. Chen, Flexoelectricity in solids: progress, challenges, and perspectives, Prog. Mater. Sci. (2019) 100570, doi: 10.1016/j.pmatsci.2019.05.003.
- [20] L.L. Ma, W.J. Chen, Y.L. Liu, B. Wang, Y. Zheng, On the mechanisms of tip-force induced switching in ferroelectric thin films: the crossover of depolarization, shear strain and flexoelectricity, J. Phys. Condens. Matter. 31 (2019), doi: 10.1088/1361-648X/aafdf2.
- [21] Y. Cao, A. Morozovska, S.V. Kalinin, Pressure-induced switching in ferroelectrics: phase-field modeling, electrochemistry, flexoelectric effect, and bulk vacancy dynamics, Phys. Rev. B. 96 (2017) 184109, doi: 10.1103/PhysRevB.96.184109.
- [22] W. Chen, J. Liu, L. Ma, L. Liu, G.L. Jiang, Y. Zheng, Mechanical switching of ferroelectric domains beyond flexoelectricity, J. Mech. Phys. Solids. 111 (2018) 43–66, doi: 10.1016/j.jmps.2017.10.011.
- [23] H. Lu, D.J. Kim, C.W. Bark, S. Ryu, C.B. Eom, E.Y. Tsymbal, A. Gruverman, Mechanically-induced resistive switching in ferroelectric tunnel junctions, Nano Lett. 12 (2012) 6289–6292, doi: 10.1021/nl303396n.

- [24] P. Sharma, S. Ryu, J.D. Burton, T.R. Paudel, C.W. Bark, Z. Huang, E.Y.Tsymbal Ariando, G. Catalan, C.B. Eom, A. Gruverman, Mechanical tuning of LaAlO3/SrTiO3 interface conductivity, Nano Lett. 15 (2015) 3547–3551, doi: 10.1021/acs.nanolett.5b01021.
- [25] M.H. Yusuf, A. Gura, X. Du, M. Dawber, Local control of the resistivity of graphene through mechanically induced switching of a ferroelectric superlattice, 2D Mater. (2017) 4. doi: 10.1088/2053-1583/aa636f.
- [26] others H. Lu, B. Wang, T. Li, A. Lipatov, H. Lee, A. Rajapitamahuni, R. Xu, X. Hong, S. Farokhipoor, L.W. Martin, C.B. Eom, L.Q. Chen, A. Sinitskii, A. Gruverman, C.B. Eom, L.Q. Chen, A. Sinitskii, A. Gruverman, Nanodomain engineering in ferroelectric capacitors with graphene electrodes, Nano Lett. 16 (2016) 6460–6466, doi: 10.1021/acs.nanolett.6b02963.
- [27] S. Das, B. Wang, Y. Cao, M. Rae Cho, Y. Jae Shin, S.M. Yang, L. Wang, M. Kim, S.V. Kalinin, L.Q. Chen, T.W. Noh, Controlled manipulation of oxygen vacancies using nanoscale flexoelectricity, Nat. Commun. 8 (2017) 1–8, doi: 10.1038/ s41467-017-00710-5.
- [28] S.M. Park, B. Wang, S. Das, S.C. Chae, J.S. Chung, J.G. Yoon, L.Q. Chen, S.M. Yang, T.W. Noh, Selective control of multiple ferroelectric switching pathways using a trailing flexoelectric field, Nat. Nanotechnol. 13 (2018) 366–370, doi: 10.1038/ s41565-018-0083-5.
- [29] M.M. Yang, D.J. Kim, M. Alexe, Flexo-photovoltaic effect, Science 360 (80) (2018) 904–907, doi: 10.1126/science.aan3256.
- [30] Z. Wen, X. Qiu, C. Li, C. Zheng, X. Ge, A. Li, D. Wu, Mechanical switching of ferroelectric polarization in ultrathin BaTiO₃ films: the effects of epitaxial strain, Appl. Phys. Lett. 042907 (2014) 1–6, doi: 10.1063/1.4863855.
- [31] A. Gómez, J.M. Vila-Fungueiriño, R. Moalla, G. Saint-Girons, J. Gázquez, M. Varela, R. Bachelet, M. Gich, F. Rivadulla, A. Carretero-Genevrier, Electric and Mechanical Switching of Ferroelectric and Resistive States in Semiconducting BaTiO₃-δFilms on Silicon, Small 13 (2017) 1–10, doi: 10.1002/smll.201701614.
- [32] A. Alsubaie, P. Sharma, G. Liu, V. Nagarajan, J. Seidel, Mechanical stress-induced switching kinetics of ferroelectric thin films at the nanoscale, Nanotechnology 28 (2017) 075709, doi: 10.1088/1361-6528/aa536d.
- [33] E.J. Guo, R. Roth, S. Das, K. Dörr, Strain induced low mechanical switching force in ultrathin PbZr_{0.2}Ti_{0.8}O₃ films, Appl, Phys. Lett. 105 (2014) 0–5, doi: 10.1063/ 1.4889892.
- [34] H. Lu, S. Liu, Z. Ye, S. Yasui, H. Funakubo, A.M. Rappe, A. Gruverman, Asymmetry in mechanical polarization switching, Appl. Phys. Lett. (2017) 110, doi: 10.1063/ 1.4983381.
- [35] L. Chen, Z. Cheng, W. Xu, X. Meng, G. Yuan, J. Liu, Z. Liu, Electrical and mechanical switching of ferroelectric polarization in the 70nm BiFeO₃film, Sci. Rep. 6 (2016) 19092, doi: 10.1038/srep19092.
- [36] T. Jia, H. Kimura, Z. Cheng, H. Zhao, Switching of both local ferroelectric and magnetic domains in multiferroic Bi_{0.9}La_{0.1}FeO₃thin film by mechanical force, Sci. Rep 6 (2016) 31867, doi: 10.1038/srep31867.
- [37] D.J. Kim, T.R. Paudel, H. Lu, J.D. Burton, J.G. Connell, E.Y. Tsymbal, S.S.A.A. Seo, A. Gruverman, Room-temperature ferroelectricity in hexagonal TbMnO₃ thin films, Adv. Mater. 26 (2014) 7660–7665, doi: 10.1002/adma.201403301.
- [38] T. Jia, H. Kimura, Z. Cheng, H. Zhao, Y.-H.H. Kim, M. Osada, T. Matsumoto, N. Shibata, Y. Ikuhara, Mechanical force involved multiple fields switching of both local ferroelectric and magnetic domain in a Bi₅Ti₃FeO₁₅ thin film, NPG Asia Mater. 9 (2017) e349 - 9, doi: 10.1038/am.2017.3.
- [39] H.W. Shin, J.Y. Son, Flexoelectric switching characteristics depending on crystallinity of highly c-oriented epitaxial SrBi₂Nb₂O₉ thin film, J. Alloys Compd. 788 (2019) 311–317, doi: 10.1016/j.jallcom.2019.02.161.
- [40] U. Celano, M. Popovici, K. Florent, S. Lavizzari, P. Favia, K. Paulussen, H. bender, L. Di Piazza, J. Van Houdt, wilfried W. Vandervorst, Flexoelectric Effect in Aldoped Hafnium Oxide, Nanoscale 10 (2018) 8471–8476, doi: 10.1039/ C8NR00618K.
- [41] X. Chen, X. Tang, X.Z. Chen, Y.L. Chen, X. Guo, H.X. Ge, Q.D. Shen, Nonvolatile data storage using mechanical force-induced polarization switching in ferroelectric polymer, Appl. Phys. Lett. 106 (2015) 042903, doi: 10.1063/1.4906859.
- [42] R. Cai, B. Nysten, Z. Hu, A.M. Jonas, Local polarization switching in stressed ferroelectric polymers, Appl. Phys. Lett. 110 (2017) 202901, doi: 10.1063/1.4983609.
- [43] G.D. Belletti, S.D. Dalosto, S. Tinte, Strain-gradient-induced switching of nanoscale domains in free-standing ultrathin films, Phys. Rev. B - Condens. Matter Mater. Phys. 89 (2014) 174104, doi: 10.1103/PhysRevB.89.174104.
- [44] J. Ocenásek, H. Lu, C.W. Bark, C.B. Eom, J. Alcalá, G. Catalan, A. Gruverman, Nano-mechanics of flexoelectric switching, Phys. Rev. B Condens. Matter Mater. Phys. 92 (2015) 1–9, doi: 10.1103/PhysRevB.92.035417.
- [45] W.J. Chen, S. Yuan, L.L. Ma, Y. Ji, B. Wang, Y. Zheng, Mechanical switching in ferroelectrics by shear stress and its implications on charged domain wall generation and vortex memory devices, RSC Adv. 8 (2018) 4434–4444, doi: 10.1039/ c7ra12233k
- [46] L. Jiang, X. Xu, Y. Zhou, Y. Zhang, Q. Yang, Strain tunability of the downward effective polarization of mechanically written domains in ferroelectric nanofilms, Rsc Adv. 6 (2016) 80946–80954. doi: 10.1039/c6ra13128i.
- [47] K.J. Choi, M. Biegalski, Y.L. Li, A. Sharan, J. Schubert, R. Uecker, P. Reiche, Y.B. Chen, X.Q. Pan, V. Gopalan, L.Q. Che, D.C. Schlom, C.B. Eom, Enhancement of ferroelectricity in strained BaTiO₃thin films, Science 306 (80) (2004) 1005–1009, doi: 10.1126/science.1103218.
- [48] L.-Q. Chen, Phase-field method of phase transitions/domain structures in ferroelectric thin films: a review, J. Am. Ceram. Soc. 91 (2008) 1835–1844, doi: 10.1111/j.1551-2916.2008.02413.x.

- [49] J.-J. Wang, B. Wang, L.-Q. Chen, Understanding, predicting, and designing ferroelectric domain structures and switching guided by the phase-field method, Annu. Rev. Mater. Res. (2019) 49.
- [50] T. Yang, B. Wang, J. Hu, L.-Q. Chen, Domain dynamics under ultrafast electric-field pulses, Phys. Rev. Lett. 124 (2020) 107601.
- [51] Y. Gu, M. Li, A.N. Morozovska, Y. Wang, E.A. Eliseev, V. Gopalan, L.-Q. Chen, Flex-oelectricity and ferroelectric domain wall structures: phase-field modeling and DFT calculations, Phys. Rev. B Condens. Matter Mater. Phys. 89 (2014) 174111, doi: 10.1103/PhysRevB.89.174111.
- [52] C. Liu, J. Wang, G. Xu, M. Kamlah, T.Y. Zhang, An isogeometric approach to flexoelectric effect in ferroelectric materials, Int. J. Solids Struct. 162 (2019) 198–210, doi: 10.1016/j.ijsolstr.2018.12.008.
- [53] N.D. Sharma, C.M. Landis, P. Sharma, Piezoelectric thin-film superlattices without using piezoelectric materials, J. Appl. Phys. (2010) 108, doi: 10.1063/1.3443404.
- [54] R. Kretschmer, K. Binder, Surface effects on phase transitions in ferroelectrics and dipolar magnets, Phys. Rev. B. 20 (1979) 1065–1076, doi: 10.1103/Phys-RevB.20.1065.
- [55] A.S. Yurkov, A.K. Tagantsev, Strong surface effect on direct bulk flexoelectric response in solids, Appl. Phys. Lett. 108 (2016) 022904, doi: 10.1063/1.4939975.
- [56] A.C. Fischer-Cripps, E.F. Gloyna, W.H. Hart, Introduction to Contact Mechanics, Springer, 2000.
- [57] W. Chen, H. Ding, Indentation of a transversely isotropic piezoelectric half-space by a rigid sphere, Acta Mech. Solida Sin. 12 (1999) 114–120.
- [58] Y.L. Li, S.Y. Hu, Z.K. Liu, L.Q. Chen, Effect of substrate constraint on the stability and evolution of ferroelectric domain structures in thin films, Acta Mater. 50 (2002) 395–411, doi: 10.1016/S1359-6454(01)00360-3.
- [59] Y.L. Li, L.Q. Chen, G. Asayama, D.G. Schlom, M.A. Zurbuchen, S.K. Streiffer, Ferro-electric domain structures in SrBi₂Nb₂O₉ epitaxial thin films: electron microscopy and phase-field simulations, J. Appl. Phys. 95 (2004) 6332–6340, doi: 10.1063/11707211
- [60] J.J. Wang, P.P. Wu, X.Q. Ma, L.Q. Chen, Temperature-pressure phase diagram and ferroelectric properties of BaTiO₃ single crystal based on a modified Landau potential, J. Appl. Phys. 108 (2010) 114105, doi: 10.1063/1.3504194.
- [61] A.G.A. Zembilgotov, N.A. Pertsev, H. Kohlstedt, R. Waser, Ultrathin epitaxial ferroelectric films grown on compressive substrates: competition between the surface and strain effects, J. Appl. Phys. 91 (2002) 2247–2254, doi: 10.1063/1.1427406.
- [62] A.L. Kholkin, V.V. Shvartsman, A.Y. Emelyanov, R. Poyato, M.L. Calzada, L. Pardo, Stress-induced suppression of piezoelectric properties in PbTiO₃:la thin films via scanning force microscopy, Appl. Phys. Lett. 82 (2003) 2127–2129, doi: 10.1063/ 1.1565177
- [63] M. Algueró, A.J. Bushby, M.J. Reece, R. Poyato, J. Ricote, M.L. Calzada, L. Pardo, Stress-induced depolarization of (Pb, La)TiO₃ ferroelectric thin films by nanoindentation, Appl. Phys. Lett. 79 (2001) 3830–3832, doi: 10.1063/1.1418258.
- [64] P. Paruch, T. Tybell, J.M. Triscone, Nanoscale control of ferroelectric polarization and domain size in epitaxial Pb(Zr_{0.2}Ti_{0.8})O₃ thin films, Appl. Phys. Lett. 79 (2001) 530–532, doi: 10.1063/1.1388024.
- [65] Y.L. Li, L.Q. Chen, Temperature-strain phase diagram for $BaTiO_3$ thin films, Appl. Phys. Lett. 88 (2006) 072905, doi: 10.1063/1.2172744.
- [66] V. Nagarajan, A. Roytburd, A. Stanishevsky, S. Prasertchoung, T. Zhao, L. Chen, J. Melngailis, O. Auciello, R. Ramesh, Dynamics of ferroelastic domains in ferroelectric thin films, Nat. Mater. 2 (2003) 43–47, doi: 10.1038/nmat800.
- [67] Ma, et al., Mechanical writing of in-plane ferroelectric vortices by tip-force and their coupled chirality, Journal of Physics: Condensed Matter (2020), doi: 10.1088/1361-648X/ab4831.
- [68] S.V. Kalinin, S. Jesse, B.J. Rodriguez, J. Shin, A.P. Baddorf, H.N. Lee, A. Borisevich, S.J. Pennycook, Spatial resolution, information limit, and contrast transfer in piezoresponse force microscopy, Nanotechnology 17 (2006) 3400–3411, doi: 10.1088/0957-4484/17/14/010.
- [69] S. Jesse, B.J. Rodriguez, S. Choudhury, A.P. Baddorf, I. Vrejoiu, D. Hesse, M. Alexe, E.A. Eliseev, A.N. Morozovska, J. Zhang, L.Q. Chen, S.V. Kalinin, Direct imaging of the spatial and energy distribution of nucleation centres in ferroelectric materials, Nat. Mater. 7 (2008) 209–215, doi: 10.1038/nmat2114.
- [70] A.V. Ievlev, A.N. Morozovska, V.Y. Shur, S.V. Kalinin, Ferroelectric switching by the grounded scanning probe microscopy tip, Phys. Rev. B - Condens. Matter Mater. Phys. 91 (2015) 1–9, doi: 10.1103/PhysRevB.91.214109.
- [71] R.K. Vasudevan, N. Balke, P. Maksymovych, S. Jesse, S.V. Kalinin, Ferroelectric or non-ferroelectric: why so many materials exhibit "ferroelectricity" on the nanoscale. Appl. Phys. Rev. 4 (2017) 21302. doi: 10.1063/1.4979015.
- [72] D. Lee, T.W. Noh, Giant flexoelectric effect through interfacial strain relaxation, Philos, Trans. R. Soc. A Math. Phys. Eng. Sci. 370 (2012) 4944–4957, doi: 10.1098/ rsta.2012.0200.
- [73] R. People, J.C. Bean, Calculation of critical layer thickness versus lattice mismatch for Ge xSi1-x/Si strained-layer heterostructures, Appl. Phys. Lett. 47 (1985) 322– 324. doi: 10.1063/1.96206.
- [74] P.M.J. Marée, J.C. Barbour, J.F. Van Der Veen, K.L. Kavanagh, C.W.T. Bulle-Lieuwma, M.P.A. Viegers, Generation of misfit dislocations in semiconductors, J. Appl. Phys. 62 (1987) 4413–4420, doi: 10.1063/1.339078.
- [75] G. Sheng, J.M. Hu, J.X. Zhang, Y.L. Li, Z.K. Liu, L.Q. Chen, Phase-field simulations of thickness-dependent domain stability in PbTiO₃ thin films, Acta Mater 60 (2012) 3296–3301, doi: 10.1016/j.actamat.2012.03.003.
- [76] H.P. Sun, W. Tian, J.H. Haeni, D.G. Schlom, X.Q. Pan, Strain relaxation by misfit dislocations in nanoscale epitaxial ferroelectric BaTiO₃ films grown on SrTiO₃ Substrate, Microsc. Microanal 8 (2002) 1162–1163.

- [77] T. Suzuki, Y. Nishi, M. Fujimoto, Analysis of misfit relaxation in heteroepitaxial BaTiO $_3$ thin films, Philos. Mag. A Phys. Condens. Matter Struct. Defects Mech. Prop. 79 (1999) 2461–2483, doi: 10.1080/01418619908214294.
- [78] H. Terauchi, Y. Watanabe, H. Kasatani, K. Kamigaki, Y. Yano, T. Terashima, Y. Bando, Structural study of epitaxial BaTiO₃ crystals, J. Phys. Soc. Japan. 61 (1992) 2194–2197, doi: 10.1143/JPSJ.61.2194.
- [79] A.G. Zembilgotov, N.A. Pertsev, H. Kohlstedt, R. Waser, Ultrathin epitaxial ferroelectric films grown on compressive substrates: competition between the surface and strain effects, J. Appl. Phys. 91 (2002) 2247–2254, doi: 10.1063/1.1427406.
- [80] L. Chen, Z. Cheng, W. Xu, X. Meng, G. Yuan, J. Liu, Z. Liu, Electrical and mechanical switching of ferroelectric polarization in the 70nm BiFeO₃ film, Sci. Rep. 6 (2016) 19092, doi: 10.1038/srep19092.
- [81] D. Liu, R. Zhao, H.M. Jafri, J. Wang, H. Huang, Phase-field simulations of surface charge-induced polarization switching, Appl. Phys. Lett. 114 (2019) 112903, doi: 10.1063/1.5083126.
- [82] G. Li, X. Huang, J. Hu, W. Zhang, Shear-strain gradient induced polarization reversal in ferroelectric BaTiO₃ thin films: a first-principles total-energy study, Phys. Rev. B. 95 (2017) 1–8, doi: 10.1103/PhysRevB.95.144111.
- [83] Gao, et al., Ferroelastic domain switching dynamics under electrical and mechanical excitations, Nature Communications (2014), doi: 10.1038/ncomms4801.
- [84] Chen, et al., Atomic imaging of mechanically induced topological transition of ferroelectric vortices, Nature Communications (2020), doi: 10.1038/s41467-020-15616-y.